



1 **UAV-enabled reconnaissance and trajectory modeling**
2 **of a co-seismic rockfall in Lefkada**

3 Charalampos Saroglou^{1*},

4 Pavlos Asteriou¹

5 Dimitris Zekkos²

6 George Tsiambaos¹

7 Marin Clark³

8 John Manousakis⁴

9 ¹Department of Geotechnical Engineering, School of Civil Engineering, National Technical
10 University of Athens

11 ²Department of Civil and Environmental Engineering, University of Michigan, USA

12 ³Department of Earth and Environmental Science, University of Michigan, USA

13 ⁴Elxis Group, S.A, Athens, Greece

14 * corresponding author: saroglou@central.ntua.gr

15
16

17 **Abstract**

18 The paper presents the field evidence and the kinematical study of the motion of a
19 rock block mobilised by an earthquake-induced rockfall in Ponti area in the island of
20 Lefkada during a M_w 6.5 earthquake on 17th November 2015. A detailed field survey
21 was deployed using an Unmanned Aerial Vehicle (UAV) with an **ultra-high definition**
22 **(UHD) camera**, which **produced a high-resolution orthophoto** and a Digital Surface
23 Model (DSM) of the terrain. The sequence of impact marks from the rock trajectory
24 on the ground surface was identified using the orthophoto and verified through a
25 detailed field survey. Additionally, the earthquake characteristics were determined in
26 order to define the acceleration on the rock slope and the initial conditions of the
27 detached block. Using the impact points from the actual rockfall trajectory, an
28 analytical approach to reconstruct the trajectory was implemented, which led to some
29 insights on the coefficients of restitution. In order to match the actual trajectory, 2D
30 and 3D rockfall analyses were performed using the recommended set of parameters.



31 However, the actual trajectory could not be accurately predicted, revealing limitations
32 of existing models.

33 **Keywords**

34 Rockfall, earthquake, DEM, modelling, restitution, UAV

35 **1. Introduction**

36 Active faulting, rock fracturing and high rates of seismicity contribute to common
37 rockfall hazards in Greece. Rockfalls primarily damage roadways and houses
38 (Saroglou, 2013) and are most often triggered by rainfall and secondly seismic
39 loading. Additionally in recent years, some rockfalls have impacted archaeological
40 sites (Marinos & Tsiambaos, 2002, Saroglou et al., 2012). The Ionian Islands, which
41 includes Lefkada Island, experience frequent M_w 5-6.5 earthquakes, as well as less
42 frequent larger (up to 7.5) earthquakes. The historical seismological record is
43 particularly well constrained with reliable detailed information for at least 23 events
44 since 1612, which induced ground failures at the island of Lefkada (Papathanasiou et
45 al. 2005) and an average of a damaging earthquake every 18 years. In the recent
46 past, a M_w 6.2 earthquake occurred on August 14 2003 and was located offshore the
47 NW coast of Lefkada. Significant damage was reported, particularly in the town of
48 Lefkada, where a PGA of 0.42g was recorded. Landslides, rockslides and rockfalls
49 occurred along the western coast of the island (Karakostas et al. 2004,
50 Papathanasiou et al., 2012).

51 On November 17th 2015, an M_w 6.5 earthquake struck the island of Lefkada and
52 triggered a number of landslides, rockfalls and some structural damage. The most
53 affected area by large rockslides was the west coast of the island, especially along its
54 central and south portion which are popular tourist destinations (Zekkos et al., 2017).
55 The landslides completely covered the majority of the west coast beaches and
56 damaged access roads.



57 A rockfall in Ponti village, which lies in the southeast side of Lefkada near the Gulf of
58 Vassiliki, was triggered during this earthquake and was responsible for one of two
59 deaths caused by the earthquake. Of particular interest is the very long travel path of
60 the rock block, which was about 800 m in plan view from the point of detachment to
61 the end of its path. Near the end of the rock fall path, the block impacted a family
62 residence, penetrated two brick walls and killed a person in the house. The block
63 exited through the back of the house and came to rest in the property's backyard.

64 The Ponti village rockfall site is characteristic of earthquake induced rockfall and an
65 example of how seismically-induced rockfall impacts human activities. It also
66 exemplifies the limitations of common 2D rockfall analysis to predict specific aspects
67 of the rockfall trajectory as measured by field evidence. In order to create a highly
68 accurate model of the rockfall propagation in 2D and 3D space, the rock path and the
69 impact point on the slope was identified by a field survey. The study was performed
70 using an Unmanned Aerial Vehicle (UAV) with an ultra-high definition (UHD) camera,
71 which produced a high-resolution orthophoto and a Digital Surface Model (DSM) of
72 the terrain. The orthophoto was used to identify the rolling section and the bouncing
73 points of the rock along its trajectory. The high-resolution DSM made it possible to
74 perform kinematical rebound analysis and a 3D rockfall analysis.

75 2. Ponti rockfall - site conditions

76 The slope overhanging Ponti village is formed in limestone and has a maximum
77 height of 600 m and an average slope angle of 35° to 40° (Figure 1). The geological
78 formations at the Ponti rockfall site are limestones covered by moderately cemented
79 talus materials. The thickness of the talus materials ranges between 0.5 and 4.0 to
80 5.0 m. A few fallen limestone blocks were identified on the scree slope, with volumes
81 between 0.5 and 2 m^3 . Based on the size distribution of these rocks on the slope, the
82 average expected block volume would be in the order of 1 to 2 m^3 .



83 The rockfall release area was at an elevation of 500 m, while the impacted house at
84 an elevation of 130 m (Figure 2). The volume of the detached limestone block was
85 approximately 2 m³ and its dimensions equal to 1.4 m x 1.4 m x 1 m. There was no
86 previous rockfall incident reported for the specific slope that impacted the road or
87 house.

88 3. UAV mapping

89 3.1. Introduction

90 A quadrotor UAV (Phantom 3 professional) was deployed to reach the uphill terrain
91 that was practically inaccessible. The UAV was equipped with an Ultra-high definition
92 (UHD) 12 MP camera and has the capacity to collect 4K video. The first objective of
93 the UAV deployment was to find the initiation point of the rock and then identify the
94 rockfall path (shown in Fig. 1). A particular focus on that part of the task was the
95 identification of rolling and bouncing sections of the rockfall path. In addition, in order
96 to generate a high-resolution orthophoto of the rockfall trajectory, aerial video
97 imagery was collected, and the resulting digital surface model (DSM) was used to
98 perform rockfall analysis. Structure-from-Motion (SfM) methodologies were
99 implemented to create a 3D point cloud of the terrain and develop a 3D model by
100 identifying matching features in multiple images. Compared to classic photogrammetry
101 methodologies, where the location of the observing point is well established, SfM
102 tracks specific discernible features in multiple images, and through non-linear least-
103 squares minimisation (Westoby et al., 2012), iteratively estimates both camera
104 positions, as well as object coordinates in an arbitrary 3D coordinate system. In this
105 process, sparse bundle adjustment (Snavely et al., 2008) is implemented to
106 transform measured image coordinates to three dimensional points of the area of
107 interest. The outcome of this process is a sparse 3D point cloud in the same local 3D
108 coordinate system (Micheletti et al., 2015). Paired with GPS measurements of a
109 number of control points (in this case 10 fast-static GPS points) at the top, middle



110 and bottom of the surveyed area, the 3D model is georeferenced to a specific
111 coordinate system.

112 3.2. High-resolution Orthophoto

113 A 5cm pixel size orthophoto was generated based on the methodology outlined
114 earlier. As shown in Fig. 3, the rolling section and the bouncing locations of the rock
115 block throughout its course were identified. The rolling section is discerned as a
116 continuous and largely linear mark left in the densely vegetated terrain that is
117 indicative of the damage caused. Impact points that are part of the bouncing section
118 of the rock, are identified as circular to ellipsoidal bare earth craters with no
119 disturbance in between. The last bouncing point before impacting the house is clearly
120 identified on the paved road. The plan view ortho-imagery, along with the original
121 footage of the video collected was crucial to the qualitative identification of these
122 features. The alternative, i.e., land-based, conventional field reconnaissance was
123 practically impossible to perform in the densely vegetated and steep terrain.

124 3.3. Digital Surface Model

125 A profile section and a 10 cm Digital Surface Model (DSM) paired with the plan view
126 orthophoto were first developed (Manousakis et al., 2016) and made possible the
127 identification of terrain features such as structures, slope benches or high trees, that
128 could affect the rock's path downhill. However, this resolution of the DSM proved to
129 be not only unnecessarily high and thus difficult to manipulate in subsequent rockfall
130 analyses, but also resulted in numerical instabilities during the rockfall analyses.
131 Therefore, a downscaled 2 m DSM was produced for the rockfall analysis. This was
132 implemented through an aggregate generalization scheme where each output cell is
133 assigned the minimum of the input cells that are encompassed by that cell. In
134 addition, noise filtering and smoothing processing were implemented to reduce the
135 effect of construction elements and vegetation in the final rasterized model. Note that



136 this resolution is still higher than the resolution of DSM that are used in rockfall
137 analyses.

138 **4. Earthquake characteristics – Initial conditions**

139 **4.1. Seismic acceleration**

140 The epicenter of the earthquake according to the National Observatory of Athens,
141 Institute of Geodynamics (NOA) is located onshore near the west coast of Lefkada.
142 The causative fault is estimated to be a near-vertical strike-slip fault with dextral
143 sense of motion (Ganas et al., 2015, 2016). Based on the focal mechanism study of
144 the earthquake it was determined that the earthquake was related to the right lateral
145 Kefalonia-Lefkada Transform Fault (KLTF), which runs nearly parallel to the west
146 coasts of both Lefkada and Kefalonia island, in two segments (Papazachos et al.
147 1998, Rondoyanni et al. 2012). The previous earthquake in this zone occurred in
148 August 2003 with a magnitude of 6.2.

149 A strong motion station recorded the ground motions in the village of Vasiliki located
150 at a distance of 2.5 km from the site. The ground motion characteristics of the
151 recording are summarized in Table 1 and are presented in Figure 4, according to an
152 ITSAK preliminary report (ITSAK, 2016). In comparison with the recordings at other
153 locations in Central Ionian, it was evident that the strongest acceleration was
154 encountered in Vasiliki area.

155 **4.2. Topography effect**

156 Peak ground acceleration along the rock slope is the intensity of base shaking
157 modified by site and topographic effects (Mavrouli et al., 2009). In the present case,
158 local shaking intensity in terms of horizontal PGA was considered. The E-W
159 component of acceleration was considered for the determination of the initial
160 velocity. The peak ground acceleration (PGA) on the slope face (PGA_{sf}) was obtained
161 by linear interpolation between the acceleration at the base (PGA_b) and at the slope



162 crest (PGA_{cr}). The acceleration at the base was equal to 0.32g and thus at the crest
163 $PGA_{cr} = 1.5 PGA_b$ equal to 0.48. Therefore, the seismic acceleration on the slope at
164 the detachment point was calculated equal to 0.45 g.

165 **4.3. Assessment of rock block's initial velocity**

166 The initial horizontal velocity of the block, at the time of detachment, was calculated
167 considering equilibrium of the produced work and the kinetic energy according to
168 equation 1.

$$169 \quad v = \sqrt{2 \cdot PGA_{sf} \cdot s} \quad (1),$$

170 where PGA_{sf} is the acceleration on the slope at the location of detachment and s the
171 initial displacement of the block in order to initiate its downslope movement.

172 The initial horizontal velocity was calculated equal to 0.67 m/sec, considering a
173 displacement in the order of $s = 0.05$ m. The vertical component of the initial velocity
174 is assumed to be zero.

175 **5. Trajectory analysis**

176 In order to estimate the possible rock paths and design remedial measures,
177 simulation programs are used in design practice, which are mostly based on the
178 lumped-mass analysis model. The trajectory of a block is modelled as a combination
179 of four motion types; free falling, bouncing, rolling and sliding (Descoedres and
180 Zimmermann, 1987).

181 **5.1. Modelling the response to an impact**

182 The most critical input parameters are the coefficients of restitution (COR), which
183 control the bouncing of the block. In general, the coefficient of restitution (COR) is
184 defined as the decimal fractional value representing the ratio of velocities (or
185 impulses or energies; depending on the definition used) before and after an impact of
186 two colliding entities (or a body and a rigid surface). When in contact with the slope,



187 the block's magnitude of velocity changes according to the COR value. Hence, COR
188 is assumed to be an overall value that takes into account all the characteristics of the
189 impact; including deformation, sliding upon contact point, transformation of rotational
190 moments into translational and vice versa (Giani, 1992).

191 The most widely used definitions originate from the theory of inelastic collision as
192 described by Newtonian mechanics. For an object impacting a rocky slope (Figure 5),
193 which is considered as a steadfast object, the kinematic COR (V_{COR}) is defined
194 according to Eq. 2.

$$195 \quad v = \frac{v_r}{v_i} \quad (2)$$

196 where v is the velocity magnitude and the subscripts i and r denote the trajectory
197 stage; incident (before impact) and rebound (after impact) respectively.

198 Two different mechanisms participate in the energy dissipation process; energy loss
199 normal to the slope is attributed to the deformation of the colliding entities, and in the
200 tangential direction is due to friction between them. Therefore kinematic COR has
201 been analyzed to the normal and tangential component with respect to the slope
202 surface, defining the normal (n_{COR}) and the tangential (t_{COR}) coefficient of restitution
203 (Eq. 3 and 4 respectively).

$$204 \quad n_{COR} = \frac{v_{n,r}}{v_{n,i}} \quad (3)$$

205 and

$$206 \quad t_{COR} = \frac{v_{t,r}}{v_{t,i}} \quad (4)$$

207 where the first subscript, n or t denotes the normal or the tangential components of
208 the velocity respectively.



209 Normal and tangential COR have prevailed in natural hazard mitigation design via
210 computer simulation due to their simplicity. Values for the coefficients of restitution
211 are acquired from values recommended in the literature (Azzoni et al. 1995;
212 Heidenreich 2004; Richards et al. 2001, RocScience, 2004). Those are mainly
213 related to the surface material type and originate from experience, experimental
214 studies or back analysis of previous rockfall events. This erroneously implies that
215 coefficients of restitution are material constants. However, COR values depend on
216 several parameters that cannot be easily assessed. Moreover, the values suggested
217 by different authors vary considerably and are sometimes contradictory.

218 Usage of the lump-mass model has some key limitations; the block is described as
219 rigid and dimensionless with an idealized shape (sphere); therefore the model
220 neglects the block's actual shape and configuration at impact, even though it is
221 evident that they both affect the resulting motion.

222 **5.2. Rockfall path characteristics**

223 23 impact points were identified on the slope surface (Figure 6). Their coordinates
224 are presented in Table 2, along block's path starting from the detachment point
225 (where $x=0$).

226 The apparent dip of the slope at impact positions was measured from the
227 topographic map; on each impact point a line was set with a length twice the block's
228 mean dimension, oriented according to preceding trajectory direction. Moreover, the
229 impact point was expanded on the topographic map to a rectangular plane with a
230 side twice as much the mean dimension of the block (Figure 7). This plane was then
231 oriented so that one side coincides with the strike direction and its' vertical side
232 toward to the dip direction. Thus, direction difference, $\Delta\phi$, was measured by the
233 strike direction and the preceding path and deviation, e , was measured as the angle
234 between pre and post impact planes (Asteriou & Tsiambaos, 2016).



235 Having a detailed field survey of the trajectory path, a back analysis according to the
236 fundamental kinematic principles was performed in order to back-calculate the actual
237 COR values.

238 5.3. Kinematic analysis and assumptions

239 The 23 impact points identified on the slope comprise a rockfall path of 22 parabolic
240 segments. The vertical and horizontal length of each segment is acquired by
241 subtracting consecutive points. Since no external forces act while the block is in the
242 air, each segment lays on a vertical plane and is described by the general equation
243 of motion as:

$$244 \quad y = x \tan \vartheta - \frac{gx^2}{2v^2} \sec^2 \vartheta \quad (5)$$

245 where: θ the launch angle from the horizon and v the launch (initial) velocity (Figure
246 8).

247 Since no evidence can be collected regarding launch angle and velocity, innumerable
248 parabolas satisfy Eq. 5. However, θ is bound between $-\beta$ and 90° , so in order to
249 acquire realistic values for the initial velocity, its sensitivity for that given range was
250 addressed (Figure 9).

251 For the case presented in Fig. 9 (the first parabolic segment) it is seen that for the
252 majority of the release angles, initial velocity variation is low and ranges between 7.2
253 and 12ms^{-1} . Additionally, the relationship between release angle and initial velocity is
254 expressed by a curvilinear function, thus a minimum initial velocity value along with
255 its release angle (denoted hereafter as θ_{cr}) can be easily acquired.

256 Given the minimum initial velocity and the critical release angle for each parabolic
257 segment, the impact velocity and angle can be calculated. Afterwards, normal and
258 tangential velocity components according to the apparent dip of the impact area, are
259 calculated in order to evaluate COR values. Results are summarized in Table 3.



260 **5.4. Coefficients of restitution**

261 It is observed that v_{cor} (Table 3) is slightly greater than one in 5 out of 22 impacts.
262 According to Eq. 3, this can only be achieved when impact velocity is less than
263 rebound velocity. However, this indicates that energy was added to the block during
264 contact, which is not possible according to the law of conservation of energy. Thus,
265 impact velocity should be greater, which is possible if the launch velocity of the
266 previous impact was more than the minimum, as assumed.

267 Omitting the impacts with $V_{cor}>1$, it is observed that kinematic COR ranges between
268 0.55 and 1.0 and presents smaller variation compared to normal or tangential
269 coefficient of restitution, similar to what was previously reported in relevant literature
270 (i.e. Asteriou et al, 2012; Asteriou & Tsiambaos, 2016).

271 The considerably wide scatter of normal COR implies that the restitution coefficient
272 cannot be a material constant. Yet, in most relevant software, normal COR is defined
273 solely by the slope material. Moreover, normal COR values higher than one were
274 calculated in 11 out of the 15 remaining impacts. Normal COR higher than one have
275 been observed in both experimental (e.g. Asteriou et al., 2012) and back-analysis
276 studies (e.g. Paronuzzi, 2009). However, in relevant software normal COR values are
277 bounded between 0 and 1.

278 Moreover, it is observed in Fig. 10 that normal COR increases as the impact angle
279 reduces, similarly to previous observations by Giacomini et al. (2012), Asteriou et al.
280 (2012) and Wyllie (2014). The correlation proposed by Wyllie (2014) is also plotted in
281 Figure 11 and seems to describe consistently, but on the unconservative side, the
282 trend and the values acquired by the aforementioned analysis and assumptions.

283

284 **6. Rockfall modelling**

285 **6.1. 2-D software**



286 Initially, a deterministic 2D rockfall analysis was performed using Rocfall software
287 (RocScience, 2004). Considering an initial velocity of 0.67 m/sec, the falling rock
288 primarily rolls on the slope and stops much earlier than its actual run out distance,
289 approximately 400 m downslope from its starting point (Fig. 6; case 1). The restitution
290 coefficients were $n_{COR}=0.35$, $t_{COR}=0.85$, which represent properties of bedrock
291 outcrops according to the suggested values provided in the documentation of the
292 software. The friction angle was set to zero. If the friction angle is set to $\varphi=32^{\circ}$ (as
293 suggested by the software documentation), the rock travels downslope only 50 m.

294 A separate analysis was performed, with lower coefficients of restitution, resembling
295 that of talus material on the slope ($n_{COR}=0.32$, $t_{COR}=0.82$, $\varphi=30^{\circ}$) as proposed by the
296 suggested values provided in the documentation of the software. In this case, the
297 rock block rolled only a few meters downslope. Therefore, it is evident that the actual
298 rock trajectory cannot be simulated.

299 In order to simulate the actual trajectory as much as possible, various combinations
300 of restitution coefficients and friction angle were considered. The closest match
301 occurred for $n_{COR}=0.60$ and $t_{COR}=0.85$, while the friction angle was set to zero and no
302 velocity scaling was applied. Only in such an analysis, the rock block reaches the
303 house; with a velocity equal to $v=18$ m/s approximately (Fig. 6; case 2). According to
304 the suggested values, these values for the coefficients correspond to a bedrock
305 material (limestone).

306 In this case, the modelled trajectory is significantly different from the actual one. The
307 main difference is that the block is rolling up to 200 m downslope while the actual
308 rolling section is 400 m (as shown in Fig. 6). Furthermore the impacts on the ground
309 in the bouncing section of the trajectory are considerably different in number (14
310 versus 23) and in location from the actual ones. Finally, the bounce height of some
311 impacts seems unrealistically high.

312 6.2. 3-D rockfall analysis



313 The rockfall trajectory model Rockyfor3D (Dorren, 2012) has been used in order to
314 validate the encountered trajectory and determine the reach probability of the falling
315 rock (from the specific source area) on the impacted house.

316 The 3D analysis was based on the down-scaled 2 m resolution Digital Elevation
317 Model (DEM) that was generated from the 10 cm DSM. The terrain features such as
318 low vegetation (e.g. bushes) and the trees were removed from the DEM as they
319 affected the rock's path downhill. The following raster maps were developed for the
320 3D analysis: a) rock density of rockfall source, b) height, width, length and shape of
321 block, c) slope surface roughness and d) soil type on the slope, which is directly
322 linked with the normal coefficient of restitution, n_{COR} .

323 The slope roughness was modeled using the mean obstacle height (MOH), which is
324 the typical height of an obstacle that the falling block encounters on the slope at a
325 possibility percentage of 70%, 20% and 10% of the trajectories (according to the
326 suggested procedure in Rockyfor3D). No vegetation was considered in the analysis,
327 which favours a longer trajectory. The parameters considered in the 3D analysis for
328 the different formations are summarised in Table 4. The spatial occurrence of each
329 soil type is shown in Figure 11 and the assigned values of n_{COR} are according to the
330 Rockyfor3D manual. The values for soil type 4.1 are slightly different from soil type 4
331 (proposed in the manual), denoting talus with a larger percentage of fallen boulders.
332 The block dimensions were considered equal to 2 m^3 and the shape of the boulder
333 was rectangle. In order to simulate the initial velocity of the falling rock due to the
334 earthquake an additional initial fall height is considered in the analysis, which for this
335 case was equal to 0.5 m.

336 The energy line angles were recalculated from the simulated trajectories and it was
337 determined that the energy line angle with highest frequency (39%) was $30\text{-}31^\circ$.
338 Based on the 3D analysis no rock blocks would impact the house, although the rock



339 paths are closer to the actual trajectories compared to RocFall software. The reach
340 probability of the falling rocks, initiating from the source point, is shown in Figure 12.

341 **6.3. Lateral dispersion & Deviation**

342 Lateral dispersion is defined as the ratio between the distance separating the two
343 extreme fall paths (as seen looking at the face of the slope) and the length of the
344 slope (Azzoni and de Freitas 1995). According to Crosta and Agliardi (2004) the
345 factors that control lateral dispersion are classified in three groups: macro-
346 topography factors, factors related to the overall slope geometry; micro-topography
347 factors controlled by the slope local roughness; and dynamic factors, associated with
348 the interaction between slope features and block dynamics during bouncing and
349 rolling. Assessing the results of an experimental investigation, Azzoni and de Freitas
350 (1995) commented that the dispersion is generally in the range of 10% to 20%,
351 regardless of the length of the slope and that steeper slopes present smaller
352 dispersion. Agliardi and Crosta (2003) calculated lateral dispersion to be up to 34%,
353 via high-resolution numerical models on natural rough and geometrically complex
354 slopes.

355 Lateral dispersion cannot be defined from the actual rockfall event in Ponti since only
356 one path is available. Using the simulated trajectories from RockyFor3D, which are in
357 the 3d space (Figure 13), a lateral dispersion of approximately 60% is shown in the
358 middle of the distance between detachment point and the house. This is significantly
359 higher compared to the findings of Azzoni and de Freitas (1995) and Agliardi and
360 Crosta (2003). Moreover, based on the actual event and intuition, the lateral
361 dispersion computed by RockyFor3D is extremely pronounced. Examining Figure 13,
362 it is notable that the rock paths are severely affected by the topography factors.
363 Therefore, assessing lateral dispersion seems to be a case specific task.

364 Asteriou & Tsiambaos (2016) defined deviation (e) as the dihedral angle between the
365 pre- and post-impact planes that contain the trajectory. They found that deviation is



366 controlled by the direction difference $\Delta\phi$, the slope inclination and the shape of the
367 block. For a parallel impact (i.e. $\Delta\phi=0^\circ$) a spherical block presents significantly less
368 deviation compared to a cubical. Additionally, deviation is equally distributed along
369 the post-impact direction and reduces as the slope's inclination increases. On oblique
370 impacts the block's direction after impact changes towards the aspect of slope and
371 as $\Delta\phi$ increases this trend becomes more pronounced.

372 Figure 14 presents deviation as a function of direction difference. It is noted that for
373 parallel impacts deviation is also equally distributed along the post-impact direction.
374 As direction difference increases, deviation becomes positive, which means that the
375 change of direction is following the direction of slope's aspect. These findings are in
376 line with trends described by Asteriou & Tsiambaos (2016), but the deviation of the
377 actual trajectory is significantly lower. This can be attributed to the different
378 conditions (i.e. block shape, slope material, slope roughness, incident velocity and
379 angle, and scale) between the experimental program conducted by Asteriou &
380 Tsiambaos (2016) and the Ponti rockfall event.

381 **7. Discussion - conclusions**

382 UAV-enabled reconnaissance was successfully used for the identification of the
383 origin of the detached rock, the rockfall trajectory and the impact points on the slope,
384 emphasizing on the motion types of the trajectory (rolling and bouncing sections). A
385 drone with an ultra-high definition (UHD) camera was deployed to reach the
386 inaccessible, steep and vegetated uphill terrain. A high-resolution orthophoto of the
387 rockfall trajectory and a 10 cm DSM was prepared, which formed the basis for an
388 analytical 2D kinematic analysis and a comparison with the outcomes of 2D and 3D
389 rockfall analysis software.

390 The initial velocity of the detached rock was estimated based on site conditions and
391 amplification of the ground acceleration due to topography. It was found that the



392 estimation of the initial velocity of the blocks plays a significant role in the accurate
393 re-production of the rockfall trajectory.

394 Based on the analytical analysis performed, it was found that the coefficients of
395 restitution cannot be directly connected to the material type, nor can be considered
396 as constants. The impact angle seems to pose a consistent effect on normal COR,
397 which has been seen also in other recent relevant studies, but has not been
398 incorporated yet on analyses models.

399 Performing a 2D rockfall analysis with the set of parameters recommended by the
400 developers, was impossible to replicate the actual trajectory revealing some
401 limitations in the present formulations. In an attempt to match the actual rock path to
402 the analysis output, the friction angle of the limestone slope was considered equal to
403 zero. However, the falling rock rolled on the slope and stopped much earlier than its
404 actual runout distance while the impacts on the ground in the bouncing section of the
405 trajectory were considerably different in number and in location compared to the
406 actual ones.

407 Using the 3D analysis software, some rock trajectories better approximated the
408 actual trajectory using the suggested values by the software developers, testifying
409 that the 3D analysis can be more accurate than the 2D analysis.

410 Based on the aforementioned analyses it becomes evident that engineering
411 judgement and experience must accompany the usage of commercial rockfall
412 software in order to acquire realistic paths. One should never rest on the suggested
413 set of parameters since the actual outcome can differ significantly, as demonstrated
414 by this case study.

415

416 **References**



- 417 1. Agliardi F, Crosta GB (2003) High resolution three-dimensional numerical
418 modelling of rockfalls. International Journal of Rock Mechanics and Mining
419 Sciences 40:455-471. doi: 10.1016/S1365-1609(03)00021-2
- 420 2. Asteriou P, Saroglou H, Tsiambaos G (2012). Geotechnical and kinematic
421 parameters affecting the coefficients of restitution for rock fall analysis.
422 International Journal of Rock Mechanics and Mining Sciences 54:103-113.
423 doi:10.1016/j.ijrmms.2012.05.029.
- 424 3. Asteriou P and Tsiambaos G. (2016). Empirical Model for Predicting Rockfall
425 Trajectory Direction. Rock Mechanics and Rock Engineering 49.3, pp. 927–
426 941.
- 427 4. Azzoni A, de Freitas MH (1995). Experimentally gained parameters, decisive
428 for rock fall analysis. Rock Mechanics and Rock Engineering 28:111-124. doi:
429 10.1007/BF01020064
- 430 5. Crosta GB, Agliardi F (2004) Parametric evaluation of 3D dispersion of
431 rockfall trajectories. Natural Hazards and Earth System Science 4:583-598.
432 doi:10.5194/nhess-4-583-2004
- 433 6. Descoedres F, Zimmermann TH. Three-dimensional dynamic calculation of
434 rockfalls. In: Proceedings of the 6th International Congress on Rock
435 Mechanics. Montreal; 30 August -3 September 1987. p. 337–42.
- 436 7. Dorren, L.K.A., 2012. Rockyfor3D (v5.1) revealed - Transparent description of
437 the complete 3D rockfall model. ecorisQ paper, 31 p.
- 438 8. Ganas, A., Briole, P., Papathanassiou, G., Bozionelos, G., Avallone, A.,
439 Melgar, D., Argyrakis, P., Valkaniotis, S., Mendonidis, E., Moshou, A. and
440 Elias, P. (2015). A preliminary report on the Nov 17, 2015 M=6.4 South
441 Lefkada earthquake, Ionian Sea, Greece, Report to EPPO, December 4
442 2015.



- 443 9. Ganas A., Elias P., Bozionelos G., Papathanassiou G., Avallone A.,
444 Papastergios P. Valkaniotis S., Parcharidis I., Briole P. (2016). Coseismic
445 deformation, field observations and seismic fault of the 17 November 2015 M
446 = 6.5, Lefkada Island, Greece earthquake. *Tectonophysics* 687, pp. 210–222.
- 447 10. Giani GP. *Rock Slope Stability Analysis*. Rotterdam: Balkema A.A; 1992.
- 448 11. Giacomini A, Thoeni K, Lambert C, Booth S, Sloan SW (2012) Experimental
449 study on rockfall drapery systems for open pit highwalls. *International Journal*
450 *of Rock Mechanics and Mining Sciences* 56:171-181.
451 doi:10.1016/j.ijrmms.2012.07.030
- 452 12. Heidenreich B (2004) Small- and half-scale experimental studies of rockfall
453 impacts on sandy slopes. Dissertation, EPFL.
- 454 13. ITSAK (2016). Preliminary presentation of the main recording of ITSAK –
455 OASP accelerometer network in Central Ionian. Earthquake M6.4 17/11/2015.
456 Thessaloniki, 11 pp.
- 457 14. Karakostas, V. G., Papadimitriou, E. E., and Papazachos, C. B. 2004.
458 Properties of the 2003 Lefkada, Ionian Islands, Greece, Earthquake Seismic
459 Sequence and Seismicity Triggering. *Bulletin of the Seismological Society of*
460 *America*, 94 (5), 1976–1981, October 2004
- 461 15. Manousakis J., Zekkos D., Saroglou H., Clark M. (2016). Comparison of UAV-
462 enabled photogrammetry-based 3D point clouds and interpolated DSMs of
463 sloping terrain for rockfall hazard analysis. *Proc. Int. Archives of the*
464 *Photogrammetry, Remote Sensing and Spatial Information Sciences*, Vol.
465 XLII-2/W2, p. 71-78.
- 466 16. Marinos P, Tsiambaos G., 2002. Earthquake triggering rock falls affecting
467 historic monuments and a traditional settlement in Skyros Island, Greece.



- 468 Proc. of the Int. Symposium: Landslide risk mitigation and protection of
469 cultural and natural heritage, Kyoto, Japan, pp. 343-346.
- 470 17. Mavrouli O., Corominas J., Wartman J. (2009). Methodology to evaluate rock
471 slope stability under seismic conditions at Sol'a de Santa Coloma, Andorra.
472 Nat. Hazards Earth Syst. Sci., 9, 1763–1773. Micheletti N., Chandler J., Lane
473 S., 2015. Structure from Motion (SfM) Photogrammetry. British Society for
474 Geomorphology. *Geomorphological Techniques*, Chap. 2, Sec. 2.2 (2015)
- 475 19. Papathanassiou, G., Valkaniotis, S., Ganas, A. and Pavlides, S. 2012. GIS-
476 based statistical analysis of the spatial distribution of earthquake-induced
477 landslides in the island of Lefkada, Ionian Islands, Greece, Landslides,
478 Journal of the International Consortium on Landslides, DOI 10.1007/s10346-
479 012-0357-1
- 480 20. Papazachos B.C., Papadimitriou E.E., Kiratzi A.A., Papazachou C.B., Louvari
481 E.K. 1998. Fault plane solutions in the Aegean sea and the surrounding area
482 and their tectonic implication. Bull Geof Teor Appl 39(3), 199–218.
- 483 21. Paronuzzi P. (2009) Field Evidence and Kinematical Back-Analysis of Block
484 Rebounds: The Lavone Rockfall, Northern Italy. *Rock Mech Rock Eng*,
485 42:783–813
- 486 22. Richards LR, Peng B, Bell DH (2001) Laboratory and field evaluation of the
487 normal Coefficient of Restitution for rocks. Proceedings of ISRM Regional
488 Symposium EUROCK2001:149-155
- 489 23. RocScience, 2004. Rocfall Manual.
- 490 24. Rondoyanni T, Sakellariou M, Baskoutas J, Christodoulou N (2012)
491 Evaluation of active faulting and earthquake secondary effects in Lefkada
492 Island, Ionian Sea, Greece: an overview. Nat Hazards 61(2), 843–860.



- 493 25. Saroglou, H. 2013. Rockfall hazard in Greece. Bulletin of the Geological
494 Society of Greece, vol. XLVII, no3, 1429-1438.
- 495 26. Saroglou, H., Marinos, V., Marinos, P., Tsiambaos, G. 2012. Rockfall hazard
496 and risk assessment: an example from a high promontory at the historical site
497 of Monemvasia, Greece. Natural Hazards and Earth System Sciences, 12,
498 1823–1836. doi:10.5194/nhess-12-1823-2012.
- 499 27. Snavely N., Seitz S.N., Szeliski R., 2008. Modeling the world from internet
500 photo collections. *International Journal of Computer Vision* 80: 189-
501 210. Westoby M.J., Brasington J., Glasser N.F., Hambrey M.J., Reynolds
502 J.M., 2012. 'Structure-from-Motion' photogrammetry: A low-cost, effective tool
503 for geoscience applications. *Geomorphology* 179 (2012) 300-314. Wyllie, D.
504 C. (2014). Calibration of rock fall modeling parameters. *International Journal*
505 *of Rock Mechanics and Mining Sciences* 67: 170-180
- 506 30. Zekkos D., Clark M., Cowell K., Medwedeff W., Manousakis J., Saroglou H.
507 Tsiambaos G. (2017). Satellite and UAV-enabled mapping of landslides
508 caused by the November 17th 2015 M_w 6.5 Lefkada earthquake. Proc. 19th Int.
509 Conference on Soil Mechanics and Geotechnical Engineering, Seoul 2017
510 (accepted for publication).
511



511

TABLES

512

Table 1. Accelerometer recordings

Component	Acceleration (cm/sec ²)	Velocity (cm/sec)	Displacement (cm)
NS-comp	363	59.3	21.27
EW-comp	327	34.1	14.01
Z-comp	256	17.7	6.56

513

514 Table 2. Impact points characteristics

Impact point	X (m)	Y (m)	app_dip (°)	$\Delta\phi$ (°)	e (°)
1	287.63	338	39.0	0	0
2	298.38	329.68	16.3	33	0
3	305.48	324.5	27.9	27	-1
4	321.54	314.83	41.0	11.6	0.5
5	365.34	287.6	30.4	11.9	0.3
6	373.32	284.85	39.7	10.6	1.8
7	425.1	261.64	14.7	6.6	-1.3
8	464.43	251.13	18.4	33.3	0.8
9	472.06	248.81	14.0	19.1	2.3
10	495.29	243.81	7.5	52.3	0.9
11	515.31	240.8	7.9	51	0.6
12	535.56	238.31	9.1	46.7	3
13	562.11	232.22	8.7	47.3	2.1
14	605.51	211.12	16.9	25.6	-1.7
15	619.1	204.48	27.1	4.6	-3
16	639.13	196.96	21.2	8	4.7
17	662.41	184	23.3	28.5	5.2
18	688.4	169.3	27.4	0.3	-2.5
19	712.23	157.67	25.4	0.5	0.1
20	745.28	143.16	21.9	0.5	-0.1
21	762.9	137.01	22.0	0.7	2
22	789.23	125.98	21.6	1.4	-0.8
23	801.53	132.75	8.4	0.2	0.1



515 Table 3. Parabolic paths characteristics for the minimum release velocity

Segment	Δx (m)	Δy (m)	θ_{cr} ($^{\circ}$)	$V_{r,min}$	V_{impact}	a_{impact} t	R	Rn	Rt
1-2	10.75	-8.33	26.8	7.19	13.19	44.5	0.55	0.71	0.31
2-3	7.1	-5.18	25.7	5.95	9.51	27.8	0.63	0.90	0.53
3-4	16.07	-9.66	31.5	9.45	12.68	9.6	0.75	3.86	0.38
4-5	43.79	-27.23	27.7	15.46	23.13	23.3	0.67	1.57	0.26
5-6	7.98	-2.75	35.7	7.47	10.49	14.9	0.71	2.52	0.30
6-7	51.78	-23.21	34.8	18.15	21.61	31.7	0.84	1.54	0.26
7-8	39.33	-10.5	35.9	17.23	24.01	36.1	0.72	0.94	0.56
8-9	7.63	-2.32	35.9	7.45	10.54	41.1	0.71	0.87	0.55
9-10	23.23	-5	40.5	13.58	13.12	30.7	1.03	1.65	0.70
10-11	20.02	-3.01	41.1	13.00	11.57	24.2	1.12	2.06	0.82
11-12	20.25	-2.49	40.9	13.26	11.22	17.6	1.18	2.94	0.82
12-13	26.55	-6.1	38.0	14.40	14.25	28.5	1.01	1.55	0.78
13-14	43.41	-21.1	32.9	16.33	25.70	40.9	0.64	0.64	0.63
14-15	13.59	-6.64	30.7	9.13	12.81	25.1	0.71	1.24	0.53
15-16	20.03	-7.52	33.8	11.67	15.42	29.8	0.76	1.33	0.42
16-17	23.27	-12.96	31.9	11.59	15.89	28.5	0.73	1.22	0.50
17-18	25.99	-14.7	29.9	12.20	20.11	30.9	0.61	0.95	0.42
18-19	23.83	-11.63	32.2	12.08	17.10	27.9	0.71	1.30	0.40
19-20	33.05	-14.51	33.6	14.55	20.62	32.1	0.71	1.14	0.43
20-21	17.62	-6.15	34.5	11.08	11.99	18.4	0.92	2.44	0.54
21-22	26.33	-11.03	35.1	13.11	16.33	27.3	0.80	1.47	0.49
22-23	12.3	6.77	58.1	14.30	13.97	48.9	1.02	1.34	0.28



516

517



517 Table 4. Restitution parameters for Rockyfor3D

Geological formation/ other	Mean n_{COR}	MOH			Soil type (Rockyfor3D)
		rg70	rg20	rg10	
Scree ($\emptyset < \sim 10$ cm), or medium compact soil with small rock fragments	0.33	0.03	0.05	0.05	3
Talus slope ($\emptyset > \sim 10$ cm), or compact soil with large rock fragments	0.38	0.05	0.1	0.2	4
Talus with fallen boulders	0.42	0.15	0.15	0.2	4.1
Bedrock with thin weathered material	0.43	0	0.05	0.1	5
Asphalt road	0.35	0	0	0	7

518



FIGURES

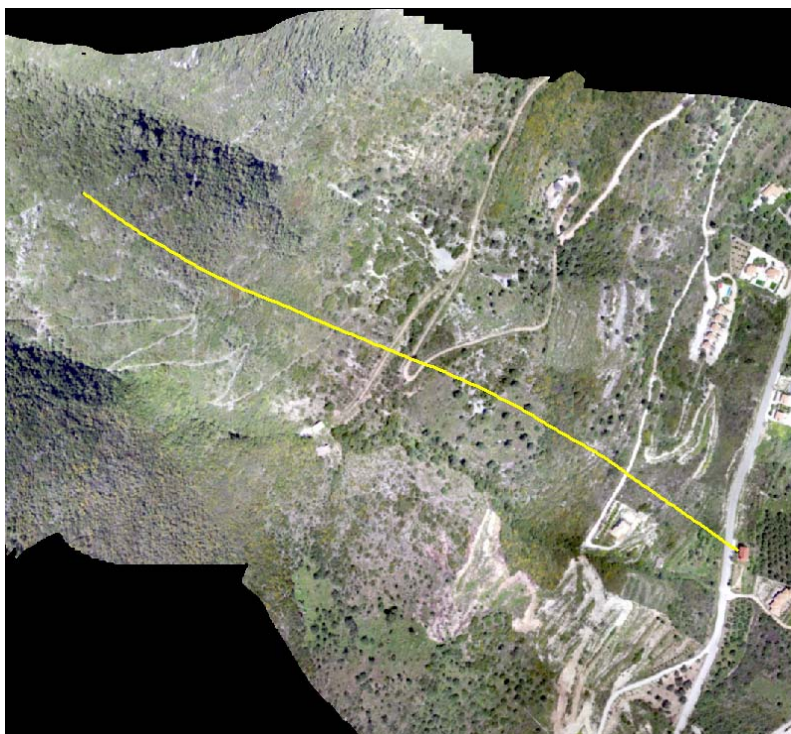


Figure 1. Orthophoto of study site showing known trajectory and impact on house.



Figure 2. Impact of rock on house in Ponti, Lefkada, Greece.

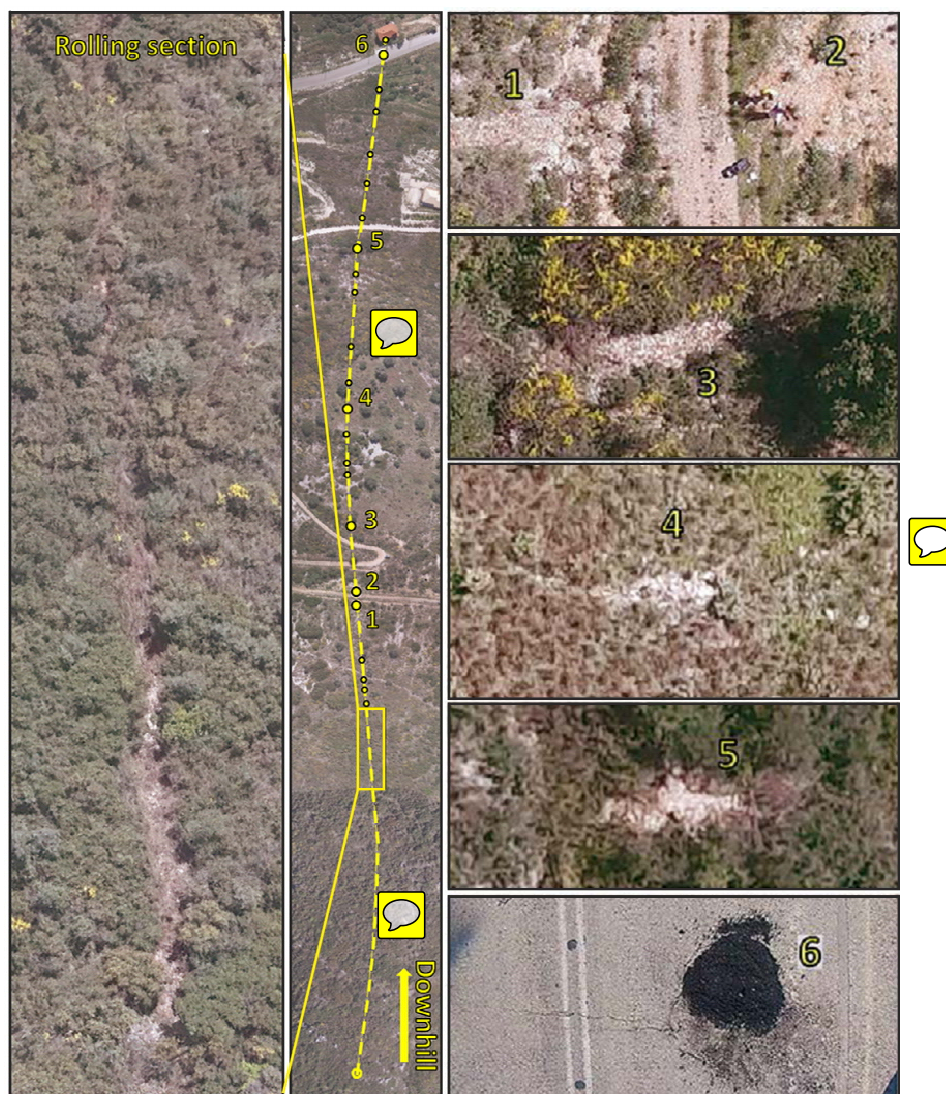


Figure 3. Top view orthophoto denoting rolling section, bouncing positions and close-ups of impact points.

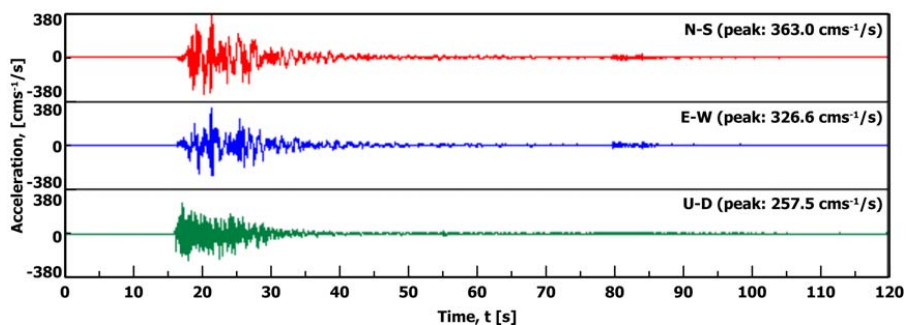


Figure 4. Acceleration recording at Vassiliki site (ITSAK, 2016)

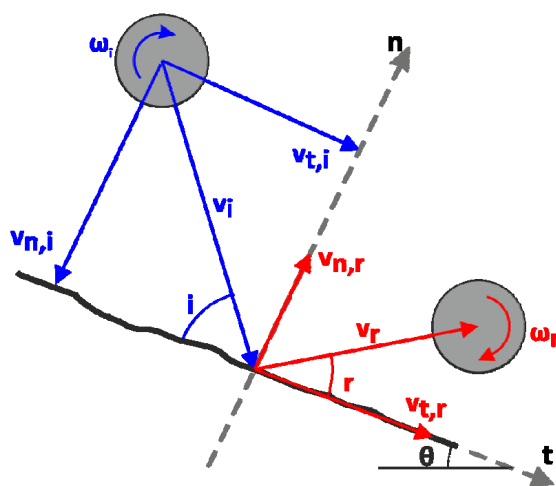


Figure 5. Coefficients of restitution

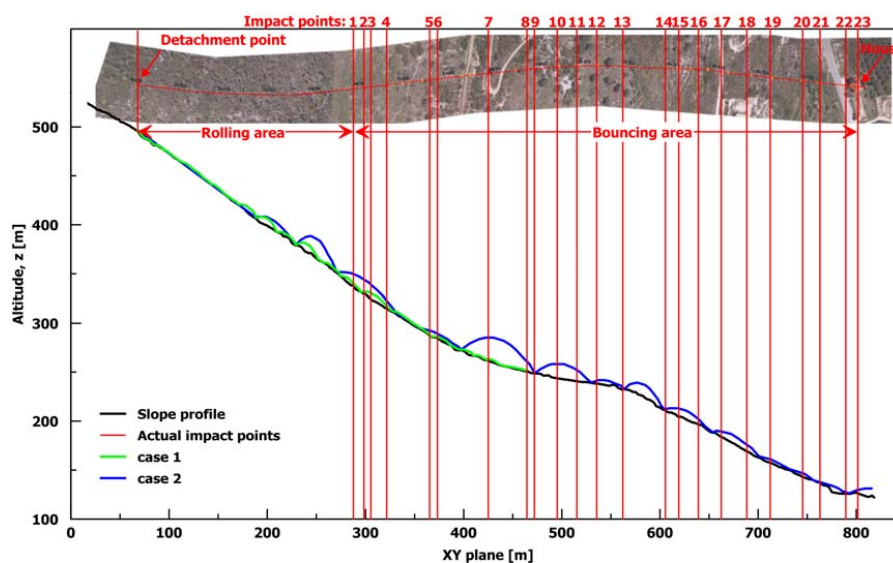


Figure 6. Plan view and cross section along block's path (units in m); 2D rockfall trajectory analysis results are plotted with green and blue line

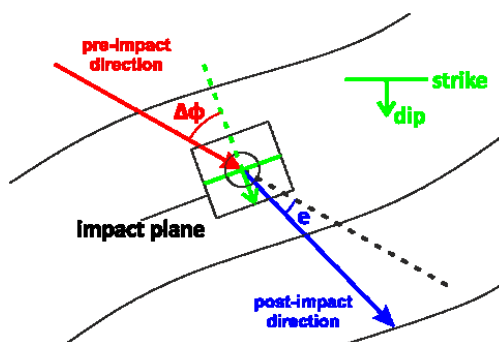


Figure 7 : Out of plane geometry

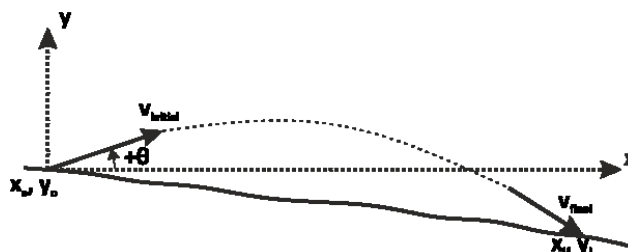




Figure 8. Parabolic segment

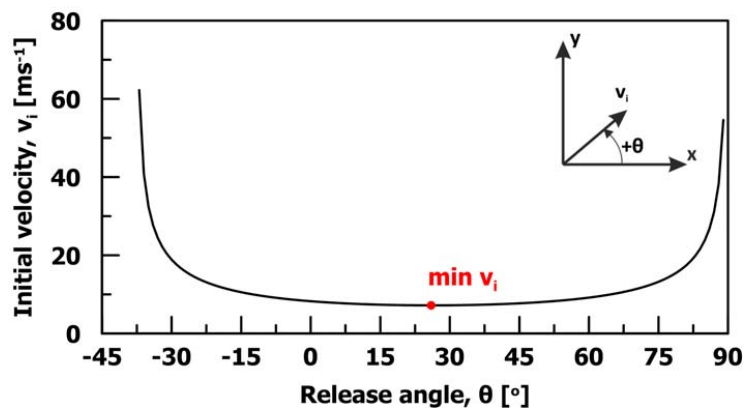


Figure 9. Release angle versus initial velocity for the first parabolic section ($\delta x=10.75\text{m}$, $\delta y=8.33\text{m}$)

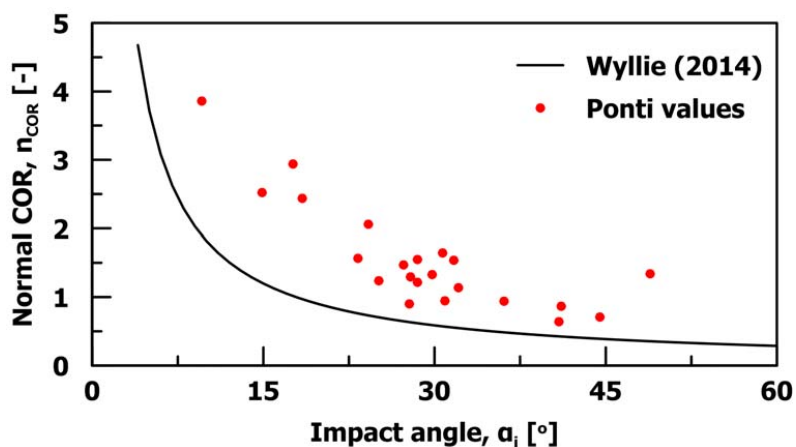
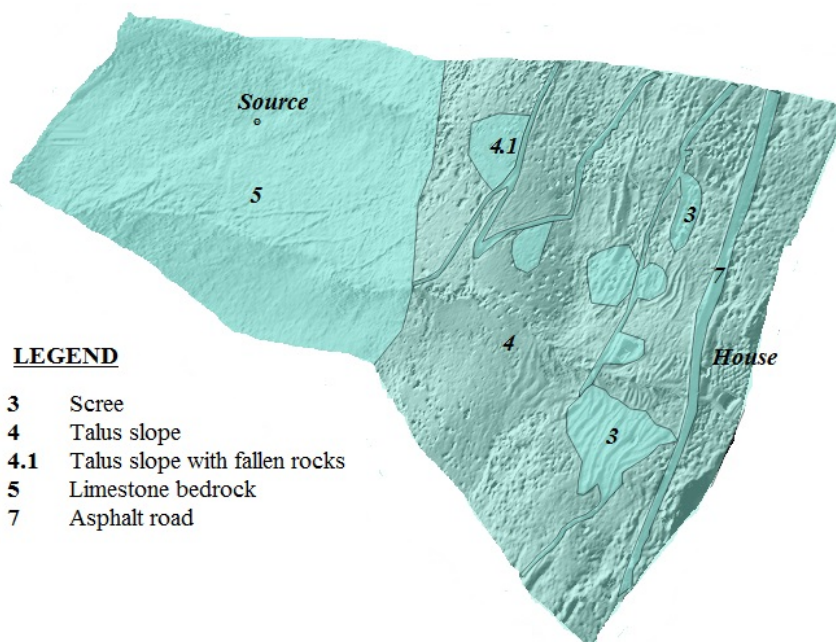


Figure 10. Normal COR versus impact angle



LEGEND

- 3 Scree
- 4 Talus slope
- 4.1 Talus slope with fallen rocks
- 5 Limestone bedrock
- 7 Asphalt road

Figure 11. Soil types for 3D rockfall analysis (according to Rockyfor3D)

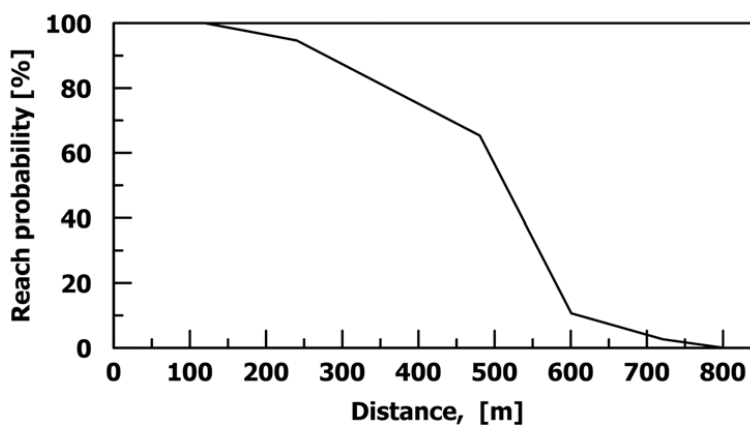


Figure 12. Reach probability graph calculated from 3D rockfall analysis

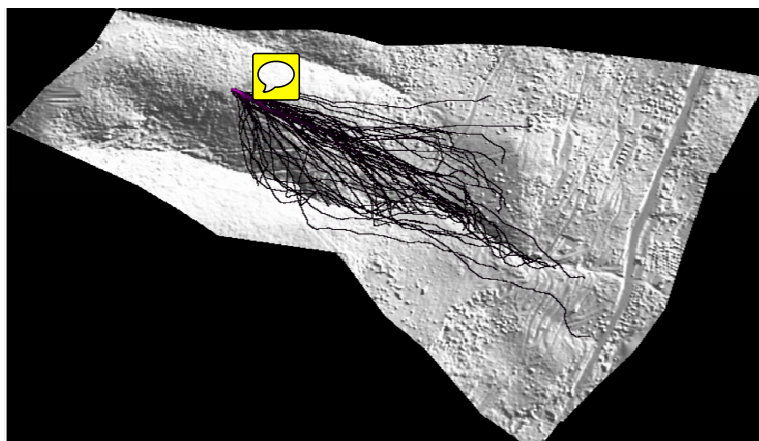


Figure 13. 3D trajectory analysis (from RockyFor3D analysis)

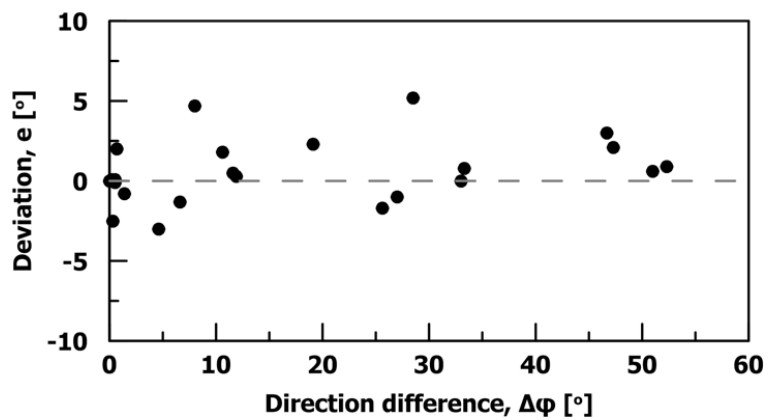


Figure 14. Deviation as a function of direction difference.